Non-linear MHD simulations of pellet triggered ELMs in JET

S. Futatani[1,2], S. Pamela[3], L. Garzotti[3], G.T.A. Huijsmans[4], M. Hoelzl[5], D. Frigione[6], M. Lennholm[3], the JOREK Team[7], JET Contributors[8]

[1]*Universitat Politècnica de Catalunya, Barcelona, Spain*
[2]*EUROfusion Consortium, JET, Culham Science Centre, Abingdon, OX14 3DB, UK*
[3]*EURATOM/CCFE, Fusion Association, Culham Science Centre, Abingdon, Oxon OX14 3DB, UK*
[4]*CEA, IRFM, F-13108, St-Paul-Lez-Durance, France*
[5]*Max-Planck-Institute for Plasmaphysics, EURATOM Association, Boltzmanstr. 2, 85748 Garching, Germany*
[6] *ENEA, C.R. Frascati, Roma, Italy*
[7]*See https://www.jorek.eu team members*
[8] *See the author list of "Overview of the JET preparation for Deuterium-Tritium Operation" by E. Joffrin et al. to be published in Nuclear Fusion Special issue: overview and summary reports from the 27th Fusion Energy Conference (Ahmedabad, India, 22-27 October 2018).*

Abstract

Non-linear MHD simulations of pellet-triggered ELMs in JET plasma have been carried out with the JOREK code. The pellet particle fueling efficiency and the power flux at the divertor target during the pellet-triggered ELM have been studied. The pellet injection in unstable plasma delivers the particle fueling but the pellet fueling rate is smaller than the rate of particle loss during the pellet triggered ELM. The JOREK simulations estimate the power flux at the divertor target and found good agreement with the experimental observation. The energy deposition of the pellet triggered ELM shows a toroidally asymmetric profile. However, and due to this toroidal asymmetry, this effect cannot be captured by the existing layout of the divertor infra-red cameras available in JET. This work highlights the benefit of having a larger number of IR cameras to analyse the heat flux for the experiments which are assumed to be toroidally asymmetric, such as the pellet and/or gas injection experiments.

1. Introduction

ITER operation is based on the H-mode regime with controlled ELMs (i.e. ELM power losses which do not cause excessive erosion of plasma facing components (PFCs)). One of the methods which is foreseen to control ELMs in ITER is based on the active controlled increase of the ELM frequency by injection of small pellets [Loarte 2014]. Experimental studies of reliable pellet ELM pacing have been demonstrated in experiments in JET, ASDEX Upgrade and DIII-D [Lang 2003, Lang 2013, Frigione 2015, Baylor 2013] for an ELM control technique to reduce the divertor heat fluxes caused by the ELMs. The key parameter of ELM control by pellet injection is the localized pressure perturbation at the plasma edge, and the physics understanding is continued to be revealed by the theoretical as well as the numerical simulations [Huysmans 2010, Futatani 2014]. It is important to understand the requirements of the pellet conditions (size, speed, etc.) on the basis of a deeper investigation of the physical mechanisms for a reliable ELM triggering.

As a contribution to a better understanding of the pellet ELM triggering, non-linear MHD modelling of pellet injection has been performed for a type I ELMy H-mode plasma in JET at 2.0 MA/2.1 T, q_{95}=3.3, NBI heating power P_{NBI}=11 MW, low triangularity $\delta_{LOW/UP}$ = 0.35/0.18 [Frigione 2015] using the non-linear MHD code JOREK [Huysmans 2009] using previously implemented neutral gas shielding (NGS) model [Gal 2008, Futatani 2014]. The

JOREK code has previously been applied to studies of spontaneous ELMs in JET [Pamela 2017] and other machines such as ASDEX Upgrade [Orain 2016] and also to pellet ELM triggering in DIII-D plasma [Futatani 2014]. JOREK solves the complex physics interaction process between the pellet ablation and the non-linear 3D MHD dynamics in a self-consistent way. This sophisticated MHD model allows to identify the key physics process governing the pellet triggered ELM and the issues related to the power fluxes to the PFCs. The pellet simulations with JOREK can estimate the particle deposition by the pellet injection and the energy loss by the pellet triggered ELM and/or spontaneous ELM. In this study, the scan of the pellet size has been carried out in order to estimate the particle deposition by the pellet injection into the unstable plasma which is just before the spontaneous ELM event. The particle and the energy release from the plasma result in heat flux onto the divertor target. This work distinguishes the features of the spontaneous ELM and the pellet triggered ELM by the distribution of the energy spectra during the ELMs. The aim of the work is to understand the physics mechanism of the ELM pacing by pellet and to estimate the power flux onto the divertor target. The validation of the simulations has been carried out with the comparison to JET data. The toroidal asymmetric profile of the power flux onto the divertor contributes to ELM mitigation in a certain toroidal angle, but it gives worse contribution in another toroidal angle as consistent with the experimental observation [Wenninger 2011]. The heat flux becomes large in a location of divertor plate, which connects to the position where the pellet triggers ELM by a magnetic field line. The position depends on the value of q_{95}. This work proposes to study the dependence of q-profile as it may be the possible control of the position of the peak of the heat flux.

In this paper, the results of the JOREK simulations of the pellet triggered ELM in a JET plasma are reported. The structure of the article is as follows. Section 2 briefly describes the simulation model. Section 2 describes the JOREK MHD modelling and the implemented pellet ablation physics. The spontaneous ELM simulation which is the reference case to be compared with the pellet triggered ELM is reported in Section 3. Section 4 shows the analysis of the simulation results and the comparison with the experimental results. The conclusion and the perspectives are discussed in Section 5.

2. Description of JOREK and the implementation of the NGS pellet ablation model

The JOREK code [Huysmans2007, Czarny2008] solves the non-linear time evolution of (extended) MHD equations in general toroidal geometry. For this paper, a reduced set of MHD equations is used as physics model. The magnetic field B and the velocity v are represented using the poloidal flux (ψ), the electric potential u and the parallel velocity $v_{||}$:

$$\vec{B} = \left(\frac{F_0}{R}\right)\vec{e}_\varphi + \left(\frac{1}{R}\right)\nabla\psi(t) \times \vec{e}_\varphi$$

$$\vec{v} = -R\nabla u(t) \times \vec{e}_\varphi + v_{||}(t)\vec{B}$$

Here, e_φ is the unit vector in toroidal direction, R is the major plasma radius and $F_0=R_0B_{\varphi 0}$ which is constant in time. Substitution in the usual visco-resistive MHD equations including diffusive particle and heat transport yields the equations to be solved for the mass density ρ, temperature T the perpendicular and parallel velocity and the poloidal flux:

$$\frac{\partial\rho}{\partial t} = -\nabla\cdot(\rho\vec{v}) + \nabla\cdot\ (D_\perp\nabla_\perp\rho) + S_\rho$$

$$\vec{e}_\varphi\cdot\nabla\times\left[R^2\left(\rho\frac{\partial\vec{v}}{\partial t} = -\rho(\vec{v}\cdot\nabla)\vec{v} - \nabla(\rho T) + \vec{J}\times\vec{B} + \mu\Delta\vec{v}\right)\right]$$

$$\vec{B}\cdot\left(\rho\frac{\partial\vec{v}}{\partial t}=-\rho(\vec{v}\cdot\nabla)\vec{v}-\nabla(\rho T)+\vec{J}\times\vec{B}+\mu\Delta\vec{v}\right)$$
$$\frac{\partial(\rho T)}{\partial T}=-\rho\vec{v}\cdot\nabla T-T\vec{v}\cdot\nabla\rho-\gamma\rho T\nabla\cdot\vec{v}+\nabla\cdot\left(\kappa_{\perp}\nabla_{\perp}T+\kappa_{\parallel}\nabla_{\parallel}T\right)+S_T$$
$$\frac{1}{R^2}\frac{\partial\psi}{\partial t}=\eta(T)\nabla\cdot\left(\frac{1}{R}\nabla_{\perp}\psi\right)-\vec{B}\cdot\nabla u \qquad (2)$$

where $D_\perp$, $\kappa_\perp$ and $\kappa_{//}=\kappa_{//0}(T/T_0)^{5/2}$ are the perpendicular particle diffusion, the perpendicular heat diffusivity and temperature dependent parallel heat conductivity, respectively. T_0 is the temperature at the plasma center, T_0=2.8 keV. $D_\perp$ and $\kappa_\perp$ are $D_\perp$=1.87 [m^2s^{-1}] and $\kappa_\perp$=1.86 [m^2s^{-1}]. S_p and S_T represent the particle and heat sources, $\eta=\eta_0(T/T_0)^{-3/2}$ is the temperature dependent plasma resistivity and μ is the viscosity modelled with the same temperature dependency as the resistivity leading to a constant Prantl number across the whole plasma. The implementation of the pellet ablation model modifies S_p with a space and time dependent density source but does not lead to a sizeable energy loss (i.e. $S_T = 0$) as the pellet ablation process is approximately adiabatic. In this work, the model does not include background plasma flows for simplicity.

In this work, we use a temperature dependent resistivity following the Spitzer dependency (see above), but increased by about a factor of 10 for computational difficulty in numerical convergence. The resistivity in the plasma center is η_0=1.86x10^{-7} [Ωm] for JOREK simulation, while the Spitzer resistivity of JET plasma is η_0=1.06x10^{-8} [Ωm]. The perpendicular and the parallel viscosities are $\mu_\perp=\mu_\parallel$= 5.39x10^{-7} [m^2s^{-1}]. The parallel heat diffusion coefficient is modelled with the correct Spitzer-Haerm temperature dependency $T^{5/2}$, but the values are reduced by a factor of 30 from values of $\kappa_\parallel^{SH}$= 3.5 x10^{10} [m^2s^{-1}] to $\kappa_\parallel$=1.18 x10^9 [m^2s^{-1}] due to the limitation of numerical calculation. The heating power used in the simulation is P_H=4.25 MW. For these simulations, the computational domain extends across the separatrix into the scrape-off layer and to (geometrically simplified) divertor targets. The boundary conditions are chosen to be those corresponding to an ideally conducting wall (all perturbations set to zero) on the surfaces parallel to the magnetic field. At the end of the open field lines, the parallel component of the velocity is set to the local sound speed in the outgoing direction (Mach-one sheath boundary condition). The boundary condition on the parallel energy flux is described by a sheath transmission factor relating the convective and conductive fluxes.

Pellet injection is considered the main technique to provide plasma fuelling in large size reactor tokamaks. In addition to fuelling, pellet injection has been found to trigger ELMs [Lang 2013] and has been adopted as ELM control scheme in ITER. In order to predict the modification to the plasma parameters and thus the pellet effective fuelling and its ELM triggering potential for ITER a model for the pellet particle source is required; for a review on pellet ablation experiments and modelling the reader is referred to [Kuteev 1995]. Among these different models such as neutral gas and plasma shielding (NGPS) [Garzotti 1997], the neutral gas shielding (NGS) model of pellet ablation [Parks 1978] is presently the one that has been more widely compared with experiment. The NGS model provides a simple relationship between the ablation rate, the pellet size, and plasma parameters [Houlberg 1988] by solving the hydrodynamic equations. In this way, the total hydrogenic particle source by the pellet along its trajectory is given by [Gal 2008]:

$$N' = 4.12\times10^{16}\cdot r_p^{1.33}\cdot n_e^{0.33}\cdot T_e^{1.64} \qquad (3)$$

where N' is the pellet ablation rate [particles/second], r_p is the pellet size (spherical size assumed) in m, n_e is the plasma electron density in (m^{-3}) and T_e is the plasma electron temperature in eV. This pellet ablation model has been implemented in JOREK. The detail information of the implementation of the pellet model in JOREK is described in Ref [Futatani 2014].

3. Simulations of spontaneous ELM in JET plasma

The simulations are based on an equilibrium reconstruction for JET discharge 84690 (q_{95}= 3.3, I_p=2.0 MA, B_T=2.1 T) [Frigione 2015]. The target plasma was a baseline H-mode scenario with NBI heating power P_{NBI}=11 MW and low triangularity $\delta_{LOW/UP}$ = 0.35/0.18. The energy confinement time was 250-300 ms. The edge transport barrier is modelled in the JOREK simulations by a suitable choice of the radial dependence of the diffusion coefficients, with reduced transport coefficients in the H-mode pedestal, leading to steady-state plasma profiles. The JOREK code builds the flux-aligned Xpoint grid, then one should run a simulation first with only the n=0 Fourier harmonic, in order to obtain a quasi-steady state which the pressure gradient has adapted to the diffusion profiles. Then, the toroidal harmonics of n=1-10 which are initialized in plasma at 'noise' level (only visible on logarithmic scale) are switched on. In this paper, "steady state" does not refer one of ELM phase of real experiment, but the starting time slice of JOREK simulation. The profiles of density and temperature during the stationary state are shown in Fig. 1. The data used in JOREK simulations is the results of fits to experimental profiles measured by the High Resolution Thomson Scattering (HRTS) diagnostics. For this analysis, we have followed the standard procedure used in JET to adjust the radial location of the experimental profiles to get 100 eV in the LCFS [Frassineti 2017].

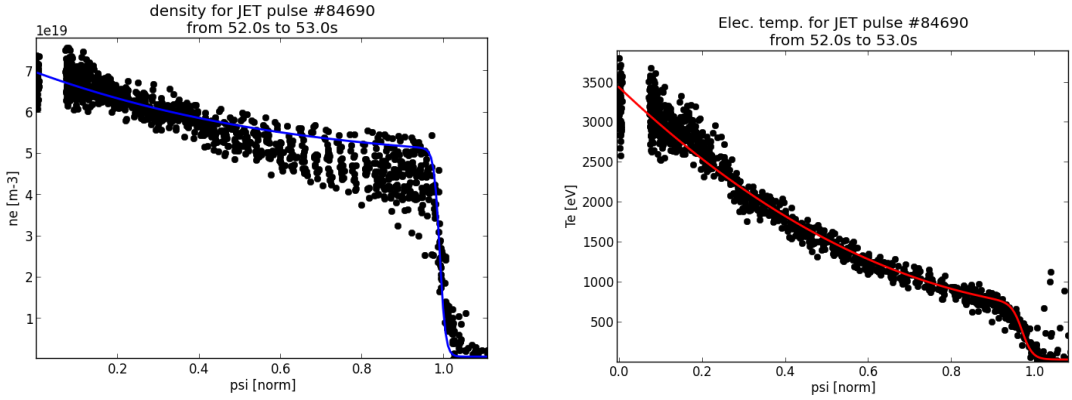

Figure 1. Density and temperature profiles modelled with JOREK (solid lines) and experimental data points from High Resolution Thomson Scattering diagnostics (black dots) versus normalized poloidal flux. The profiles refer the JET discharge #84690 [Frigione 2015].

In order to verify that these experimental profiles are indeed close to the MHD instability leading to spontaneous ELMs, JOREK simulations have been carried out without the pellet injection. The simulations of the study have been carried out using the toroidal harmonics n=0-10. Due to the limitation of computation resources, the work limits the number of toroidal harmonics up to n=10. In the realistic plasma which includes the diamagnetic flows, the high-n modes are stabilized [Mink 2018], therefore the simulations with n=0-10 are adequate to study the ELM physics. Figure 2 shows the result of a JOREK simulation, the time evolution of the magnetic and the kinetic energies of toroidal Fourier modes, n=1-10.

After the spontaneous ELM crash at t=4850μs which can be distinguished by the mode of n=10, the plasma goes to the relaxed state due to the particle and the energy release from the plasma. The duration of the spontaneous ELM which is defined by the period of the excitation of n=10 mode is about 0.2-0.5ms which is a typical time scale of the fast MHD event. After the ELM event, the n=2 mode is excited by the external kink modes at the pedestal region which is not of interest to the present work. The work aims to study the first peak of divertor power load in the time evolution and compare it with JET data, in order to exclude the influence of secondary instability which may be suppressed by inclusion of diamagnetic rotation [Orain 2015]. Figure 3 shows the plasma density and the pressure during an uncontrolled or spontaneous ELM in JET plasma at simulation time t=4850μs. The clear structures of the ballooning modes are observed at the low field side and the X-point region of the plasma.

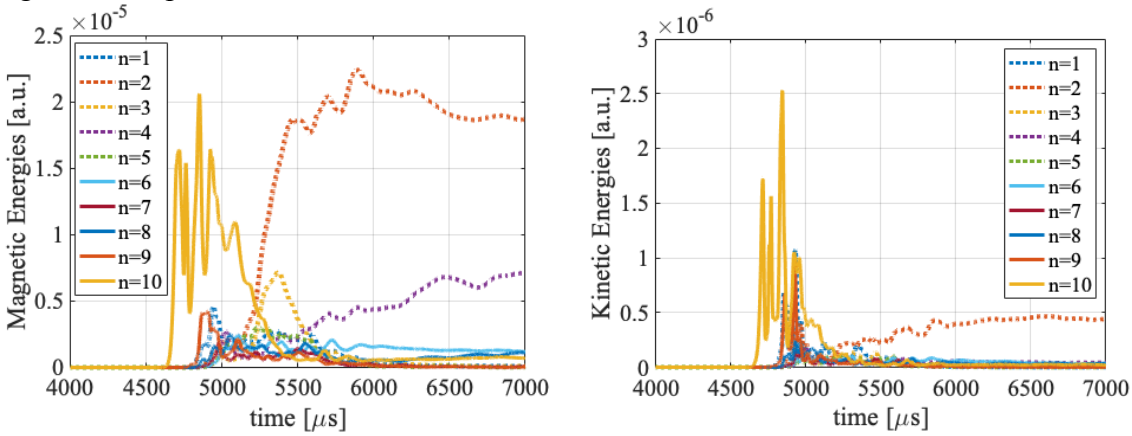

Figure 2. The magnetic and the kinetic energies of the n=1-10 toroidal harmonic as a function of time. The n=10 mode leads the ELM crash at t=4850 μs. The duration of the spontaneous ELM of the simulation is 0.2-0.5ms.

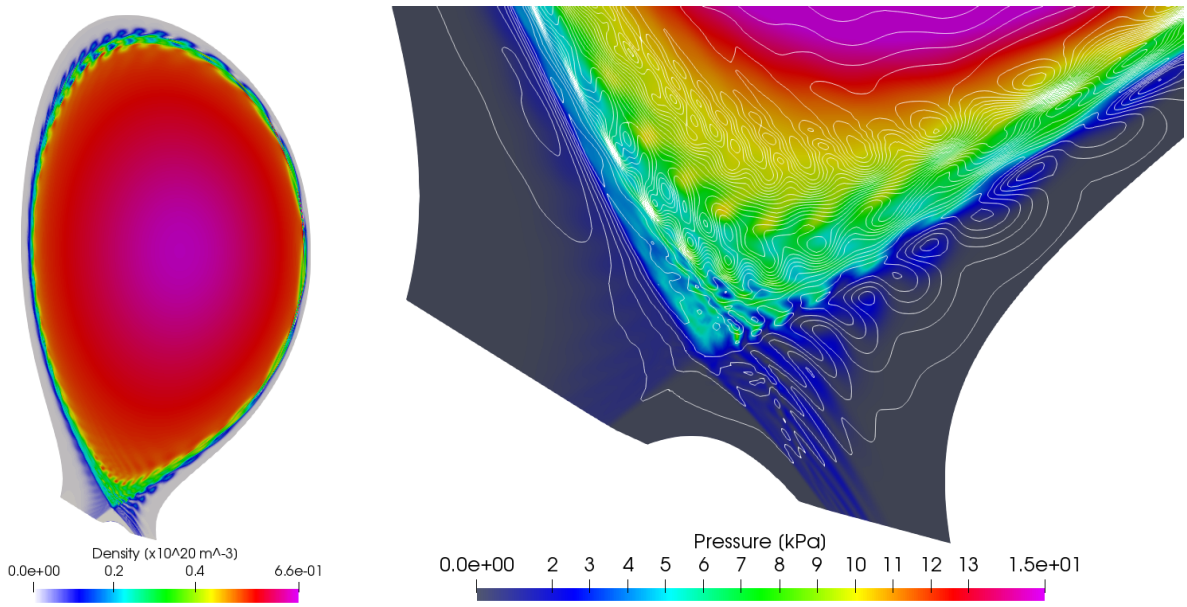

Figure 3. Plasma density (left) and pressure (right) (in colour) during an uncontrolled or spontaneous ELM in JET plasma at t=4850μs obtained in the JOREK simulations. There are clear ballooning mode structures in the separatrix region.

The energy content in the plasma versus time is shown in Fig. 4. The spontaneous ELM leads the energy loss of 4.6% of the total plasma in 0.5 ms. The experimental measurement of the considered discharge shows the average energy loss is about 100 kJ in 6 ms out of the average energy content of about 3 MJ, which corresponds to 3.3 %. Considering that the simulation gives the instant value of the ELM energy loss, the JOREK observation is comparable with the experimental measurement. The thermal energy content inside the plasma continues to drop with a reduced rate after the ELM event because the simulations do not include the stabilizing poloidal and toroidal plasma flows.

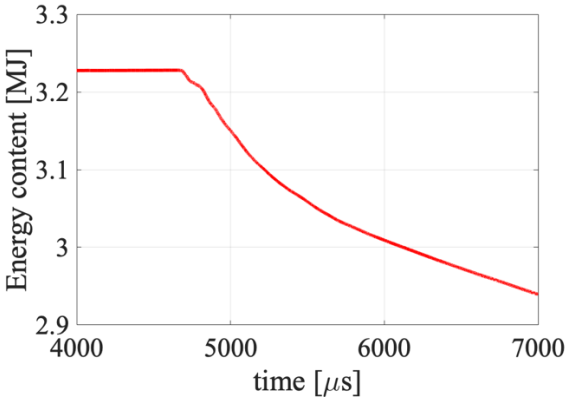

Figure 4. The time evolution of the energy content inside the separatrix. The initial fast drop within ~0.5 ms corresponds to the ELM crash. The energy loss continues afterwards with a lower rate due to the absence of stabilizing background plasma rotation in the simulations.

Figure 5 shows the density, temperature and pressure profiles versus normalized poloidal flux for several time slices. The profile at the pedestal shoulder collapses in the beginning of the ELM event, then the density and the temperature at the inner side of the pedestal (Ψ_N >0.9) are released to the outside of the separatrix. The JOREK modelling of the plasma shows the relaxation of the plasma by the spontaneous ELM with the large particle and the energy release. The diagnostics with sufficient time resolution to follow the perturbation in the edge region during an ELM event in JET are the reflectometer for the electron density profile and the ECE radiometer for the electron temperature profiles. Unfortunately, for this particular discharge the fast profile data was not available. Future work is planned to carry out a more quantitative comparison between the experimental profiles and modelling results. In the rest of the paper the focus will be on the analysis of the impact of pellet injection on the heat flux on the divertor.

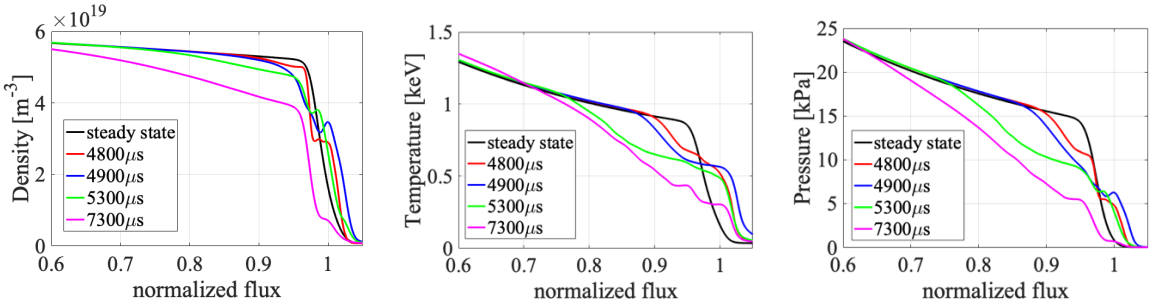

F*igure 5. Density, temperature and pressure profiles modelled with JOREK versus normalized poloidal flux along the midplane for the profiles of several time slices.*

Figure 6 shows the time evolution of the heat flux on the outer/inner divertor target at a toroidal angle of 180 degrees and 0 degree. Filamentary structures of the footprint of the heat flux on the divertor target are observed. The movement of the filaments indicates that the plasma rotates during the ELM activity (plasma rotation induced by the ELM itself due to Maxwell stress). It is important to note that the heat flux on the divertor target shows small toroidal variations during the spontaneous ELM. This observation will be the one of the key issues to be discussed in the later sections.

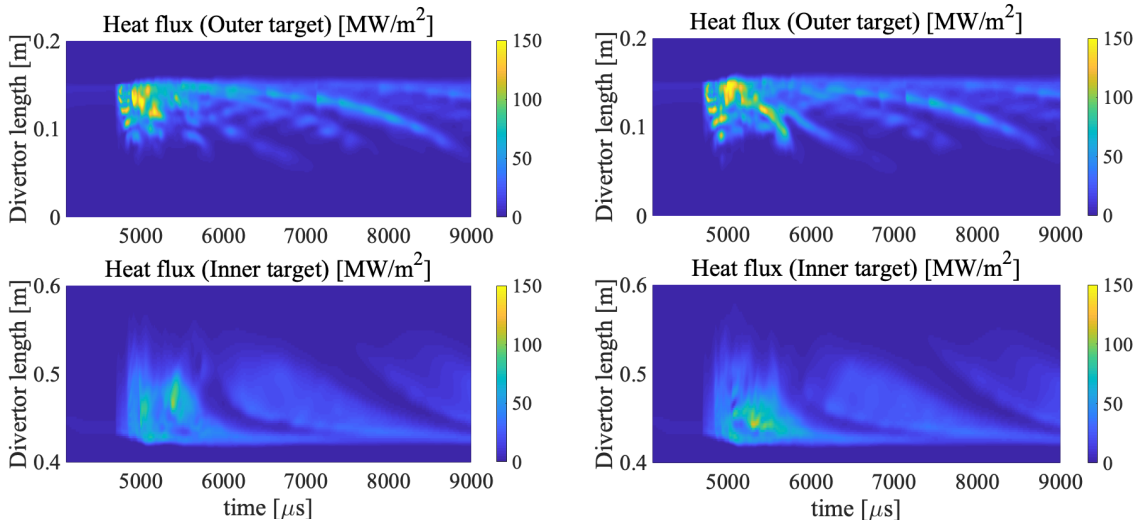

Figure 6. The time evolution of the heat flux on the outer/inner divertor target of the toroidal angle of 180º. (left panels) and 0º. (right panels). The strike point at the outer divertor is L=0.145 [m] (R=2.70 [m]), and the inner divertor target is L=0.43 [m] (R=2.44 [m]).

Figure 7.1 shows the time evolution of the power load onto the divertor and the wall. The most part of the power loads reaches to the divertor targets, the ratio of the peak power load between inner and outer target is 42% and 58%. Figure 7.2 shows the heat flux on the inner and the outer divertor target at t=5000μs (where the heat flux to the outer divertor reaches its maximum and the heat flux at the inner divertor has not yet reached comparable values due to a short time delay between both targets). The profile of the heat flux onto the inner and the outer divertor is compared at the toroidal angles of 0º and 180º. The 3D plot shows the heat flux profile versus toroidal angles. The heat flux on the divertor target shows small toroidal variations during the spontaneous ELM. The general experimental observation is that the ELM energy deposition is typically higher on the inboard side [Eich 2007]. The actual power load is nevertheless slightly higher on the inboard target but with much less asymmetry compared to the energy. The reason for this seems to be related to the different widening of the ELM foot print on the target, which is larger on the inner than on the outer divertor regions. The inclusion of the diamagnetic drifts induces a near-symmetric ELM energy deposition on the inner and outer divertor target plates [Orain 2015], but this pellet work has been carried out without diamagnetic effects due to the capacity of computing resources.

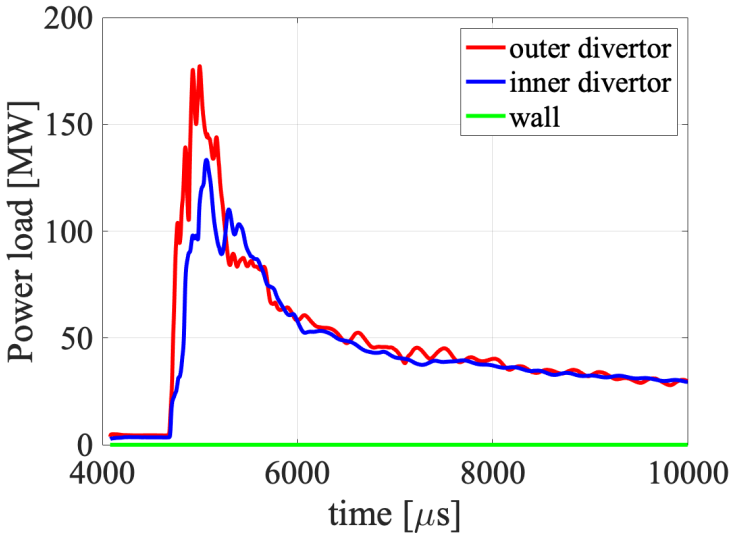

Figure 7.1. The time evolution of the power load onto the divertor and the wall. The ratio of the peak power load between inner and outer target is 42% and 58%.

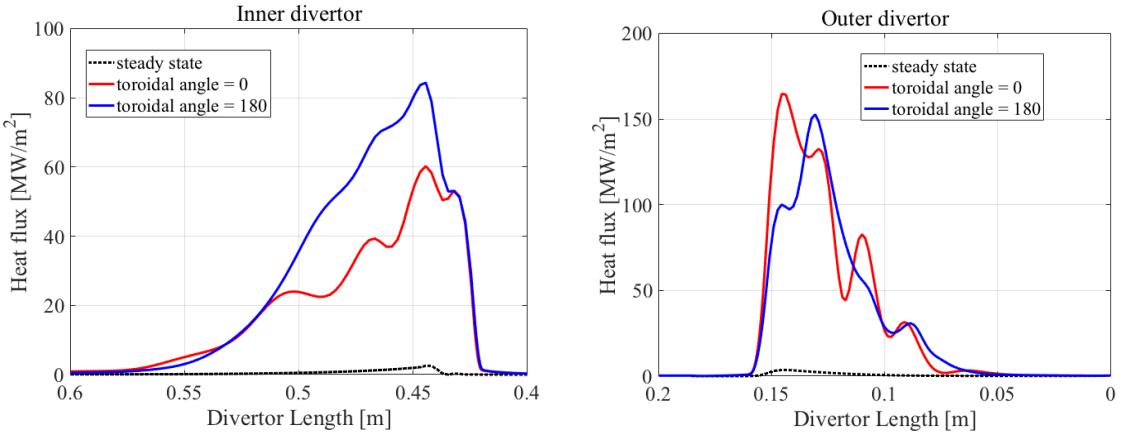

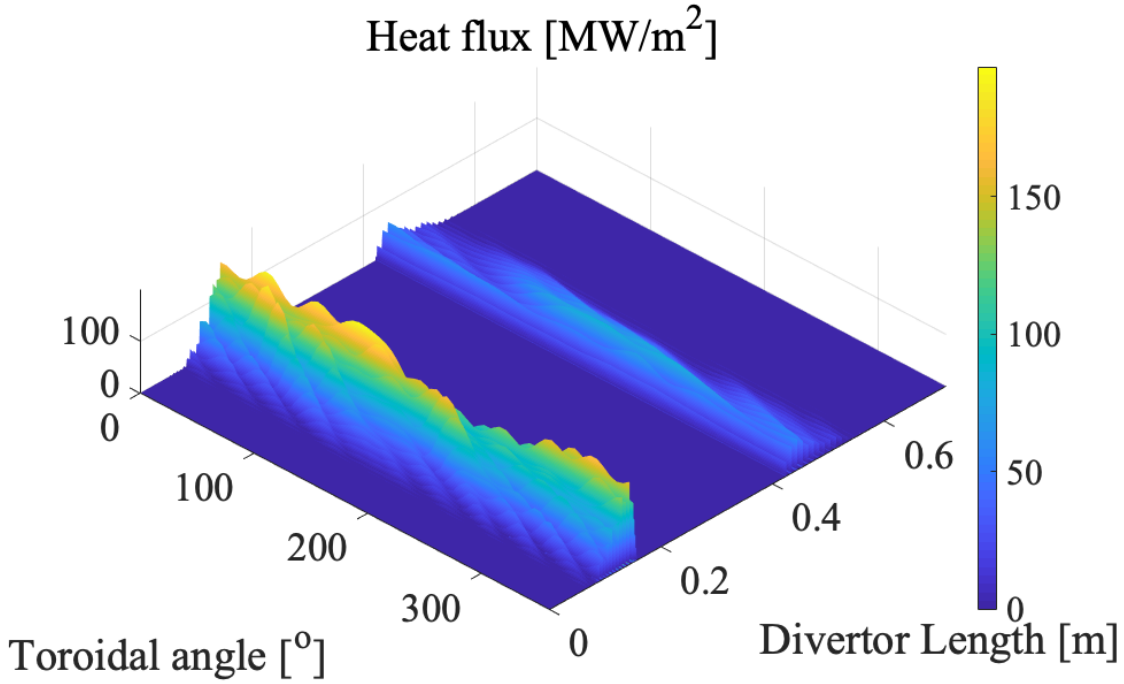

Figure 7.2. (top panels) The heat flux onto the inner/outer divertor target at the time of the largest power load onto the outer divertor target, t=5000μs. (bottom panel) The heat flux profile at that time onto the divertor targets versus the toroidal angle.

4. Pellet injection in JET plasma

4.1 Mechanism of the pellet triggered ELM

The JOREK simulations to study the non-linear growth of MHD activity leading to the triggering of ELMs by pellet injection have been carried out. The simulations are for JET discharge 84690. The efficiency of pellet triggered ELM in the experiment is calculated with the total number of pellets followed by an ELM divided by the total number of pellets injected (or rather detected in the plasma). The efficiency of the pellet ELM triggering in the discharge of the experiment is 46% for the first phase of pellets injections and 31% for the second phase. The HRTS n_e and T_e profiles (shown in Figure 1) used in this work were taken for the first phase of the pulse. In JOREK simulation, the pellet is injected at t=4106 μs when the plasma is in a quasi-steady state in Fig. 2. Therefore, we are injecting the pellet into the unstable plasma just before the spontaneous ELM would appear out of the random initial perturbation applied. In experiments, the pellets can be only launched at certain time slots, therefore the timing of the pellet is difficult to choose. The work assumes the situation that the pellet is launched just before the spontaneous ELM event. The aim of the work is to compare the heat flux onto the divertor with experimental results in terms of the variation of toroidal angle. The plasma is already unstable and an ELM would be triggered in any case. The injection of the pellet triggers an ELM earlier than the spontaneous ELM which will be discussed in Fig. 11. The simulations are performed for two pellet sizes, $0.5\text{x}10^{20}$ and $2.0\text{x}10^{20}$ particles contained in the pellet (1.1 mm and 1.7 mm of the diameter of cylindrical pellet with the same height as the diameter, respectively) injected from Low Field Side, outer-midplane (LFS-MP) of the JET plasma (see [Frigione 2015] for the detail information). They are the minimum (for $0.5\text{x}10^{20}$) and the maximum ($2.0\text{x}10^{20}$) of the pellet size capability for the pellet injector of JET. There is a loss of the particles which are contained in the pellet in the guiding tube between the pellet injector and the JET plasma. Therefore, practically in the experiment, the pellet size of '2.0×10^{20}' is nominal value, and will not contain the number of particles as indicated. The pellet is injected with speed 100m/s at t=4106 μs for all cases of pellet injection simulations. The pellet injection speed and the pellet size are chosen to be comparable with experimental situation [Frigione 2015]. The initial pellet location is outside of the separatrix where the flux surface of the separatrix is Ψ=-0.2033 and the flux surface of the pellet location is Ψ=-0.1765, where the pellet goes out from the JET LFS wall [Frigione 2015]. The distance between the separatrix and the initial pellet location is 2 cm. Figure 8 shows the density perturbation caused by the pellet ablation in the pedestal at t=4295 μs. The toroidally and the poloidally localized pellet density source creates the density perturbation at the pellet location.

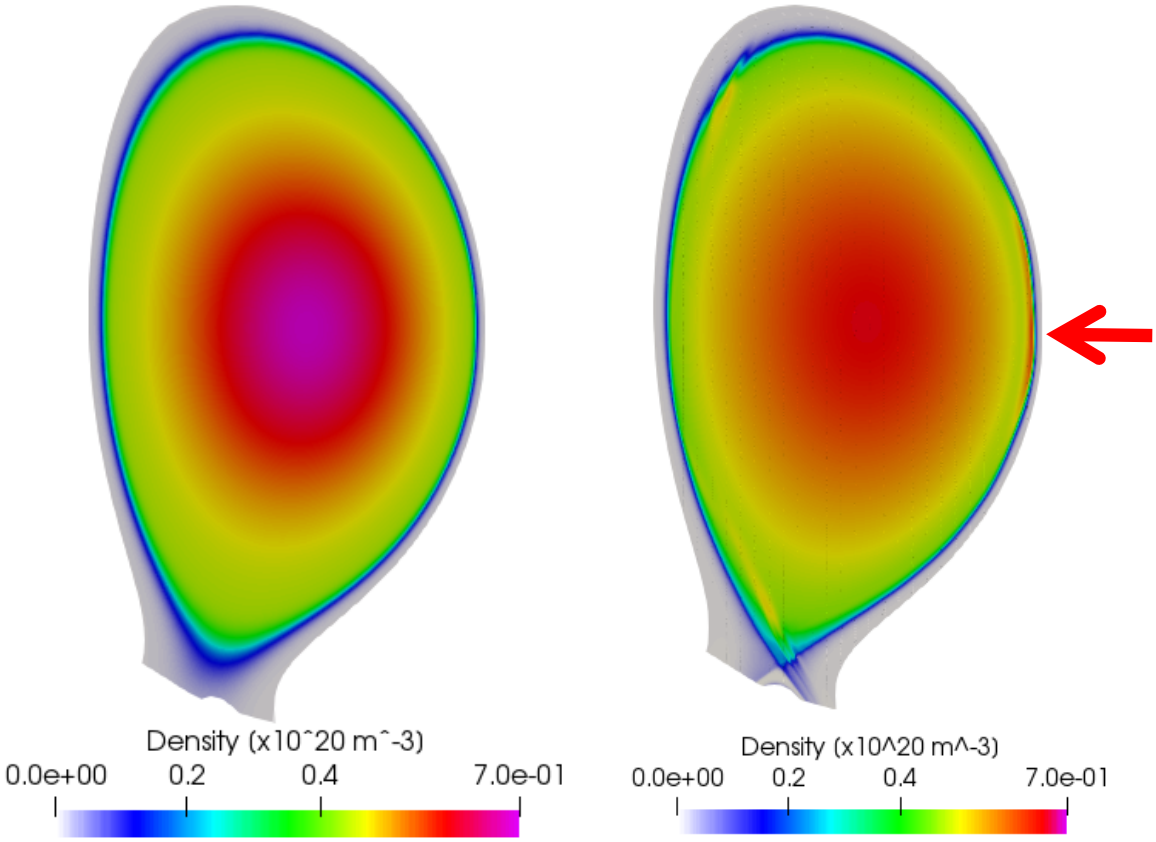

Figure 8. The density contour at (left panel) t=4106μs and (right panel) the pellet cloud in the pedestal at t=4295 μs, after 189μs of the pellet injection time t=4106μs. The pellet is injected from Low Field Side (LFS) of the JET plasma with the injection velocity of 100 m/s.

JOREK simulations show that the physics of pellet ablation in the plasma leads to a complex time-varying three-dimensional MHD phenomenology which affects the physics of the ablation of the pellet itself. The pellet ablation is adiabatic and, as it proceeds, the locally created high density region created by the ablation of the pellet expands along field lines with the local sound speed as shown in Fig. 9a. On a shorter timescale, electron conduction along the field lines reheats this high density region and leads to an increase of the plasma pressure in the toroidally and poloidally localised high density structure created by pellet ablation and expansion along the field lines. The localized pressure perturbation gives rise to the growth of MHD activity. When the pellet is small which leads to a small pressure perturbation, the plasma can relax after the pellet ablation process is terminated and the localized plasma over-pressure is re-distributed by plasma transport process. When a pellet large enough to cross the stability limit of the plasma is injected, the MHD response grows strongly corresponding to the triggering of an ELM. The key parameter of the pellet triggered ELM is three-dimensionally localized pressure perturbation, i.e. plasma is three-dimensionally modified. In a similar manner to RMPs (Resonant Magnetic Perturbations), there is so far no linear MHD stability code that can evaluate the MHD stability of the plasma with a 3D perturbation. The pellet excites the plasma rotation in the counter-clockwise direction which affects the MHD stability which will be discussed in Section 4.2. Figure 9b shows the density contour plot on the last flux surface during the pellet triggered ELM. The very localized excitation of ballooning modes is observed along the magnetic field which is on the location of the pellet ablation. The ballooning mode structures extends

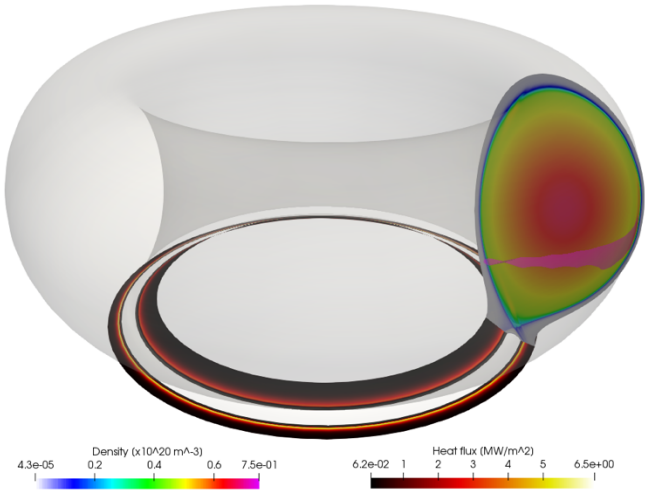

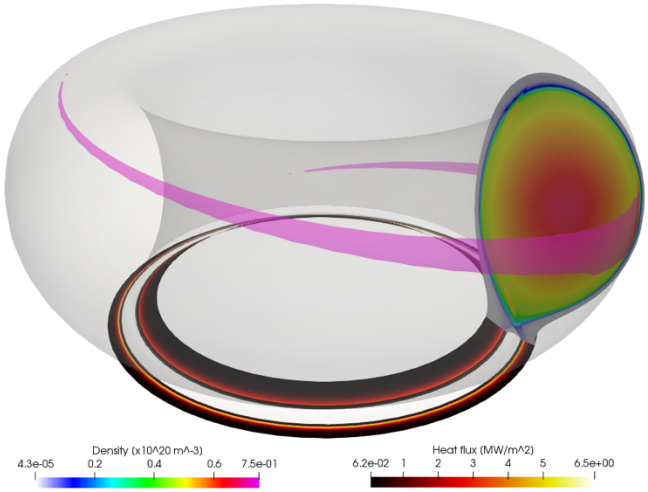

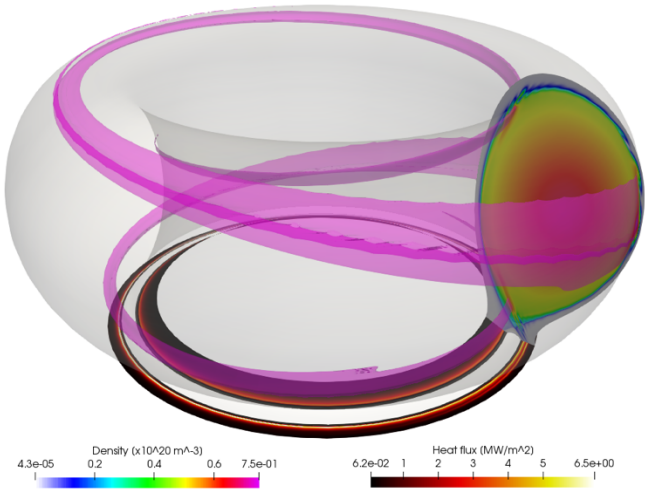

over the whole area of the pedestal region as the simulation evolves in time, and the ELM crash occurs. The toroidal axisymmetry is broken by the pellet injection. This leads to an increase of the toroidal asymmetry of the power flux onto the divertor target which will be discussed in Section 5.2.

Figure 9a. The 2.0x10^{20}D pellet is injected from outer midplane into the plasma. The expansion of the pellet cloud which is shown in a pink band for 20 μs, 50 μs, 80 μs after the pellet injection time t=4106μs. We visualize the pellet cloud by highlighting the density contour corresponding to 5.8x10^{19} [m^{-3}].

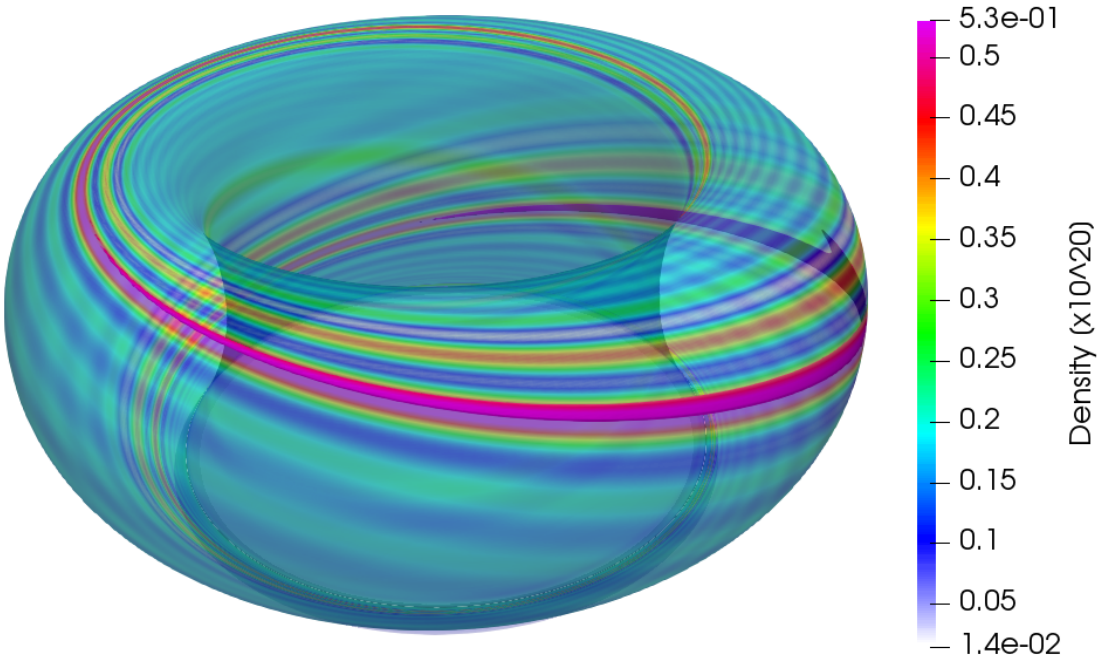

Figure 9b. The 2.0x10^{20}D pellet is injected from the outer midplane into the plasma which is very unstable already without the pellet perturbation. The localized ballooning mode structures appear along the magnetic field lines which are at the pellet location.

4.2 The dependence of the pellet size in JET plasma

The simulations of two pellet sizes, 0.5x10^{20} and 2.0x10^{20} particles contained in the pellet (1.1 mm and 1.7 mm of the diameter of cylindrical pellet with the same height as the diameter, respectively) injected from Low Field Side, outer-midplane (LFS-MP) of the JET plasma are described in the following. They are the minimum and the maximum of the pellet size for the pellet injector of JET. The pellet is injected from outside of the separatrix with 100 m/s at t=4106 μs for all cases of this study.

Figure 10 shows the pellet ablation rate versus time and versus normalized flux for two pellet sizes, 0.5x10^{20}D and 2.0x10^{20}D. The behaviour of the pellet ablation rate strongly increases when the pellet goes into the plasma. The ablation rate of the 2.0x10^{20}D case changes at t=4390μs. This is due to the pellet triggered ELM which accompanies the relaxation of the temperature profile. The pellet ablation rate which is strongly influenced by the local temperature at the pellet location becomes significantly small due to the lower plasma temperature which is resulted by the ELM event. The decrease of the pellet ablation rate results that the pellet remains until t= 4927μs. For the same reason, the 2.0x10^{20}D pellet penetrates the pedestal and reaches deeper of the plasma.

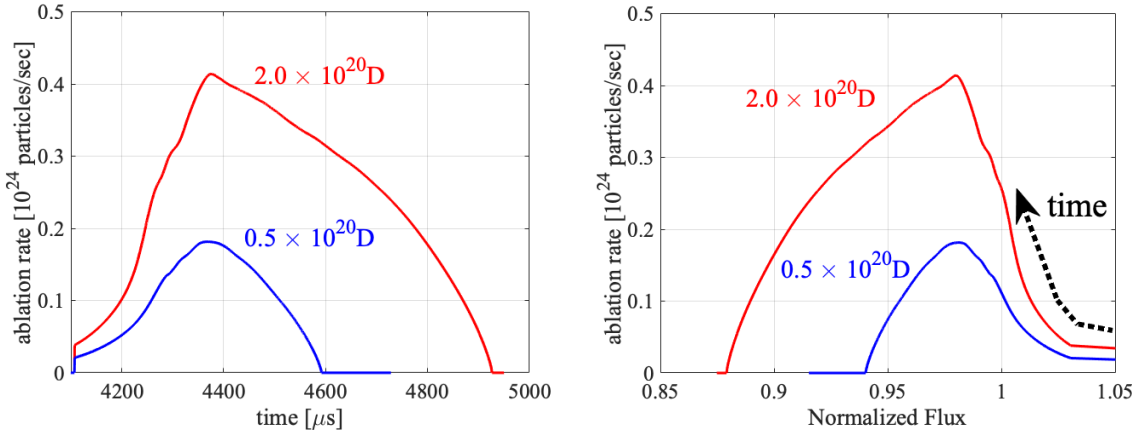

Figure 10. The pellet ablation rate versus time (left panel) and versus normalized flux (right panel) for the dependence of the pellet size, $0.5x10^{20}$ and $2.0x10^{20}$ particles contained in the pellet (1.1 and 1.7 mm of the diameter of cylindrical pellet with the same height as the diameter, respectively) injected from Low Field Side, outer-midplane (LFS-MP) of the JET plasma.

The pellet injection is started together with the introduction of the toroidal harmonics (n=0-10). The magnetic energies grow quickly just after the pellet injection, as shown in Fig. 11.

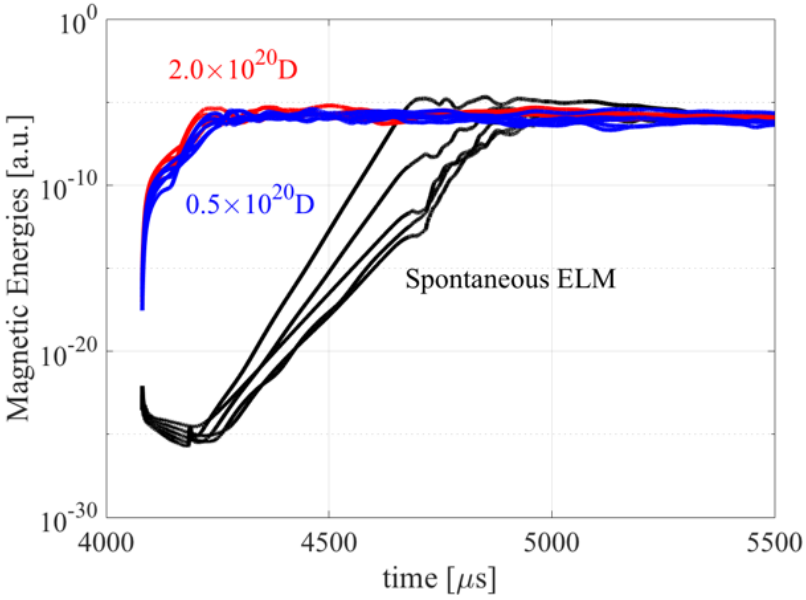

Figure 11. Time evolution of magnetic energies of high toroidal modes, n=6-10 for the spontaneous ELM (black lines) and pellets of $0.5x10^{20}$ (blue lines) and $2.0x10^{20}$ (red lines) particles in the pellet.

The JOREK simulations show that, as already illustrated in Fig. 9, the ablation of the pellet leads to a growth of the MHD activity as reflected by the growth of kinetic and magnetic energy of the n=6-10 modes. Note that JOREK solves the self-consistent electromagnetic physics, therefore the magnetic energies grow according to the kinetic energy growth. The amplitude of the magnetic energy and the kinetic energy increases with pellet size, as shown in Fig. 12a. Figure 12b shows for the magnetic and kinetic energies the sum over all toroidal

modes included in the simulation (n=1-10) respectively, with the sum over the higher mode numbers (n=6-10). The amplitude of the high toroidal modes of the pellet triggered ELM is smaller than the ones of the spontaneous ELM. As shown in Fig. 12-a and Fig. 12-b, the pellet triggers ELM at t~4370 μs, after 120 μs of pellets go across the separatrix. After the ELM crash (spontaneous ELM and pellet triggered ELM), the localized plasma over-pressure is re-distributed by plasma transport process. The relaxation of the modes is very slow which is in the time scale of the transport. The high-n ballooning mode of MHD activity is dominant during the ELM crash. This could be due to the lack of diamagnetic effects in these simulations, which would suppress high-n ballooning modes and allow lower-n modes to be more dominant during the crash. In order to compare simulation results with experimental observation, such as [Perez von Thun 2019], further studies would require the use of diamagnetic effects in the simulations, which is beyond the scope of this current work.

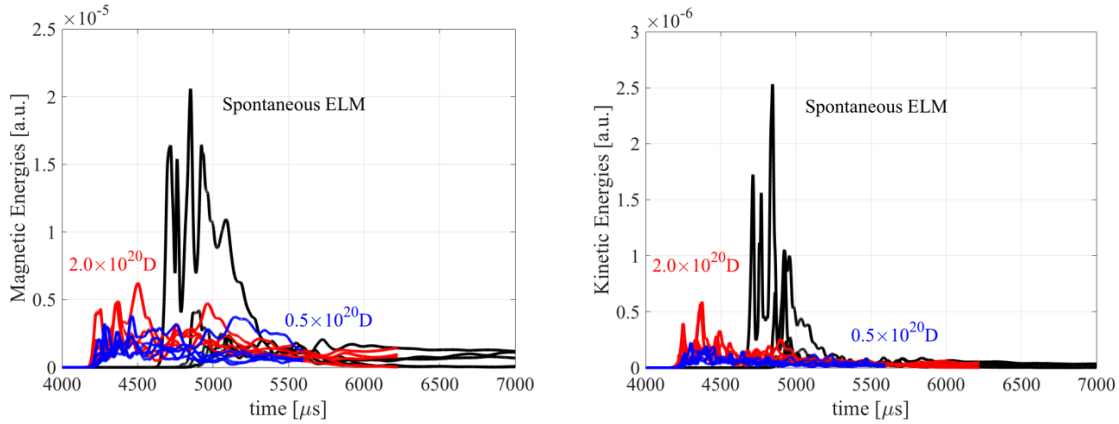

Figure 12-a. Time evolution of magnetic energies (left) and kinetic energies (right) of high toroidal modes, n=6-10 for the spontaneous ELM, and two pellet sizes of 0.5x10^{20} and 2.0x10^{20} particles in the pellet.

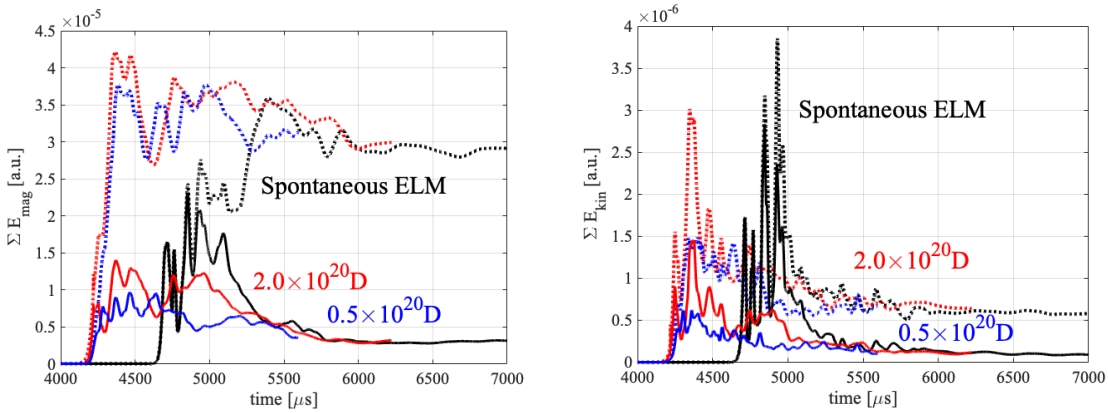

Figure 12-b. Time evolution of the integration of the magnetic energies (left) and kinetic energies (right) of n=6-10 (solid lines) and n=1-10 (dashed lines) for the spontaneous ELM, and two pellet sizes of 0.5x10^{20} and 2.0x10^{20} particles in the pellet.

Figure 13 shows the density, temperature and pressure profiles versus pellet trajectory at their maximum ablation rate. The amplitude of the density perturbation due to the pellet ablation is positively correlated to the injected pellet size. As a consequence, the amplitude

of the pressure perturbation is also correlated to the injected pellet size, in a same manner with the density perturbation.

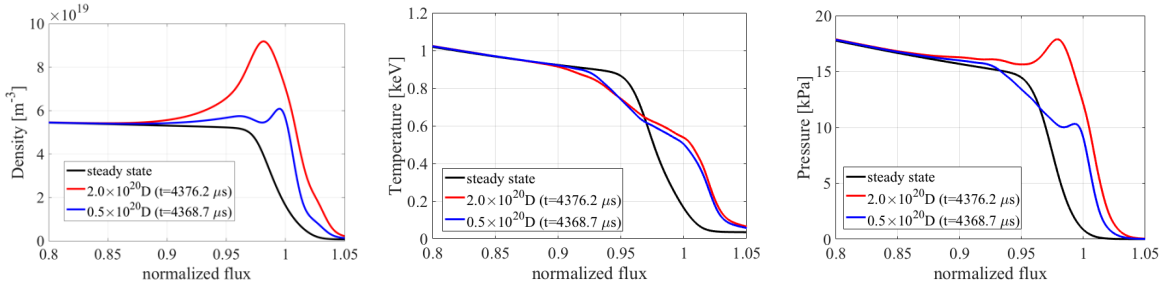

Figure 13. The profiles of the density, temperature, pressure at their maximum ablation rate.

Figure 14 shows the time evolution of the density, temperature and pressure profiles versus pellet trajectory during the injection of the pellets of 2.0x10^{20}D and 0.5x10^{20}D at various different time points. The injected pellet creates the density perturbation. The density perturbation increases according pellet ablation which is given by the function of the local temperature and density in Eq. (3). The amplitude of the perturbation of the density is the largest at the maximum ablation rate. After the pellet ablation beyond the maximum ablation, the pellet ablation decreases leading to the decrease of the density perturbation. The evolution of the pressure perturbation shows the same behaviour with the density perturbation due to the ELM behaviour. The pellet excites MHD activities after the pellet goes across the separatrix. In the ablation process, the ballooning mode structures evolve at the separatrix region. In this process, the density and temperature profiles fluctuate forming structures and the temperature profile looks increase at the separatrix. Thereafter, pellet triggers ELM at t~4370 μs. The particles are released from the plasma, leading the profiles relaxation of the density and pressure. Due to the particle release by the ELM, the density increases outside Ψ_N>0.95.

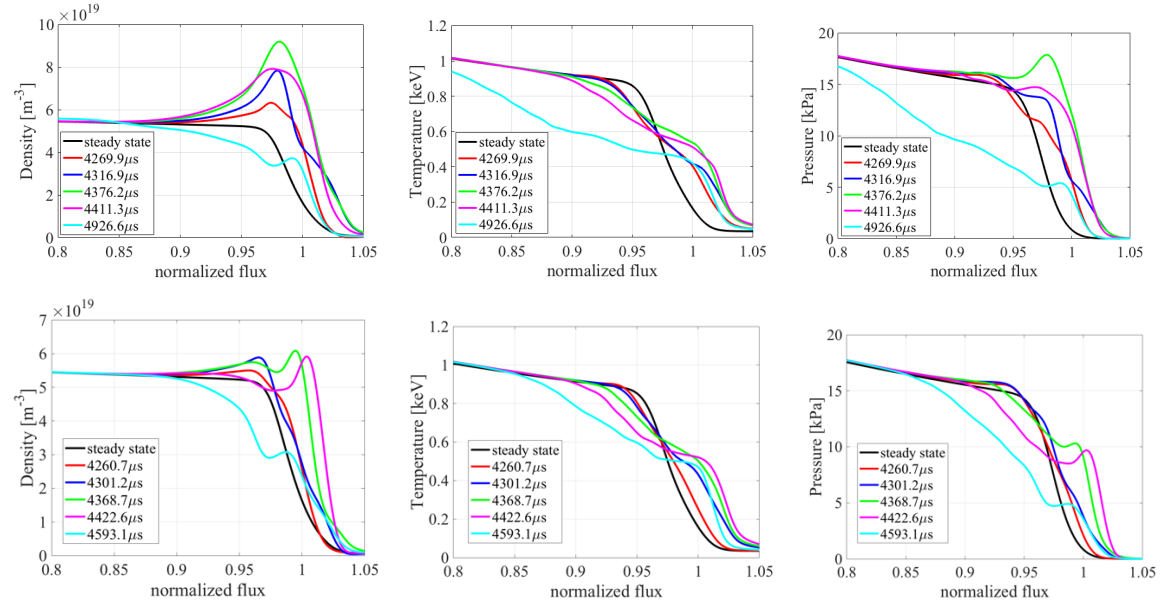

Figure 14. The profiles of the density, temperature, pressure after the injection of the pellet 2.0x10^{20}D (top panels) and 0.5x10^{20}D (bottom panels) at various different time points during the injection.

Figure 15 shows the plasma density contours for pellet injected at the LFS-MP of a JET plasma for several time slices. The formation of ballooning mode structures in the density contours for the pellet size is indicative of the triggering of an ELM. The plasma rotation in the counter-clockwise direction is observed in the density perturbation. This is the same feature driven by Maxwell stress as the spontaneous ELM behaviour [Huysmans2009]. The excited plasma rotation by pellet triggered ELM affects the MHD stability [Aiba 2017].

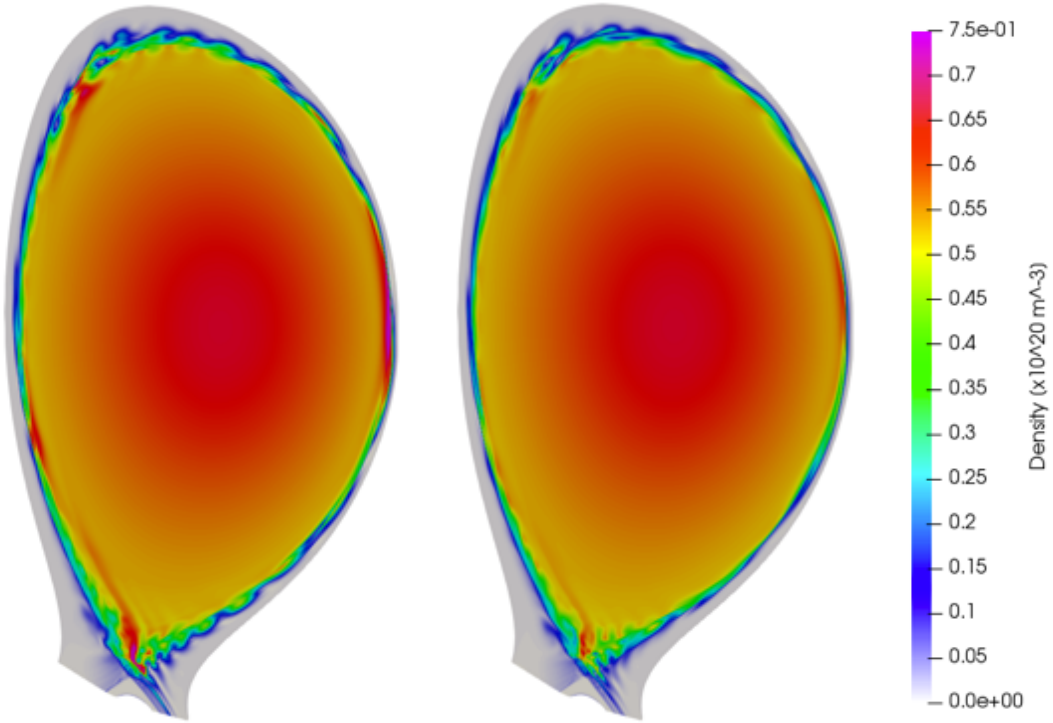

Figure 15. Plasma density contours for pellets injected at the LFS-MP of JET plasma with two pellet sizes; (left panel) 2.0x10^{20}D and (right panel) 0.5x10^{20}D at their maximum ablation rate, t=4376μs and t=4368μs, respectively. The formation of ballooning mode structures in the density contours is indicative of the triggering of an ELM.

The spectrum of the toroidal modes during the ELM has been compared as shown in Fig.16. The spectrum is time-averaged over the ELM event, for the spontaneous ELM (4680-5150μs) and the pellet triggered ELMs (4280-4550μs). The distribution of the spectra is different between the spontaneous and the pellet triggered ELMs. The kinetic energies spectrum of the spontaneous ELM shows the dominance of high-n modes. The lower n modes and the higher n modes are the dominant in the spontaneous ELM, therefore the distribution shows hollow profile of the spectra distribution versus toroidal modes. On the opposite, the spectra of the pellet triggered ELM show the low-n modes are dominant and the spectra are homogeneously distributed over the whole toroidal modes. The simulations have been performed up to n=10 due to the limited computing resources, but the difference would be expected to find in the higher toroidal modes (~n=30 or n=40) which will be performed in the future. However higher n modes would also be stabilized when background ExB and diamagnetic drifts are included, which is also planned for the near future.

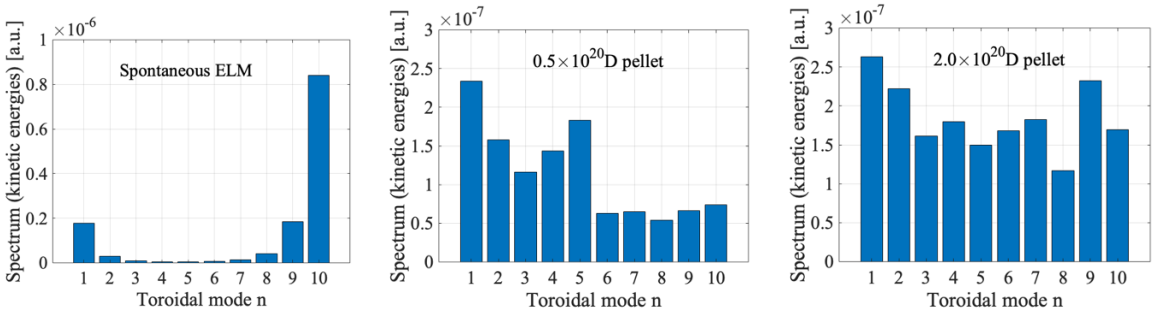

Figure 16. The spectrum of kinetic energies versus the toroidal modes n for the spontaneous ELM (left panel) and the pellet triggered ELM of 0.5x10^{20}D pellet (middle panel) and 2.0x10^{20}D pellet (right panel).

In order to evaluate the spatial and temporal characteristics of the heat and particles fluxes associated with the injection of pellets for ELM triggering a set of simulations have been carried out which include the full plasma cross section including the separatrix and SOL region. Figure 17a shows the particle content inside the separatrix versus time. The thermal energy content inside separatrix is shown in Fig. 17b. The small pellet (0.5x10^{20}D) triggers an ELM and the particle and energy are released from the plasma. The pellet delivers the particle fueling but the fueling rate is smaller than the rate of particle loss during the ELM event. Therefore, the particle content inside separatrix of the small pellet (0.5x10^{20}D) does not show the increase of the particle content in the plasma. The large pellet (2.0x10^{20}D) has larger ablation rate and longer lifetime of the pellet than the small pellet (0.5x10^{20}D), therefore the increase of the particle content inside separatrix is observed. However, a lot more particles from the pellet are released by the ELM, therefore the final particle content after the plasma seems lower than before. The pellet delivers the particle fueling but the fueling rate is smaller than the rate of particle loss during the ELM event. As a consequence, the effect of pellet fueling is not visible in the pellet injection into an unstable plasma. The energy loss versus time which is in Fig. 17b shows that the pellet triggers an ELM much before the crash of the spontaneous ELM. This is due to the fast growth of the excited MHD mode by the pellet injection and the plasma reaches the threshold of the ELM crash before the spontaneous ELM.

Figure 18 shows the integrated power load over the plasma facing component versus time. The power load which is led by the spontaneous ELM and the large pellet, 2.0x10^{20}D shows up to 270 MW at the peak. The small pellet, 0.5x10^{20}D shows the 240 MW of the peak power load. The behaviour of the time evolution of the power load onto the PFCs shows a small difference between the spontaneous ELM and the pellet triggered ELM. After the pellet triggered ELM, the localized plasma over-pressure is re-distributed by plasma transport process. During the transport process, the excited modes relax slowly. Therefore, the power load onto the PFCs by pellet triggered ELM is higher than the spontaneous ELM for t=0-2000 μs. After t=2000 μs from the ELM onset, the same drop of the plots is observed.

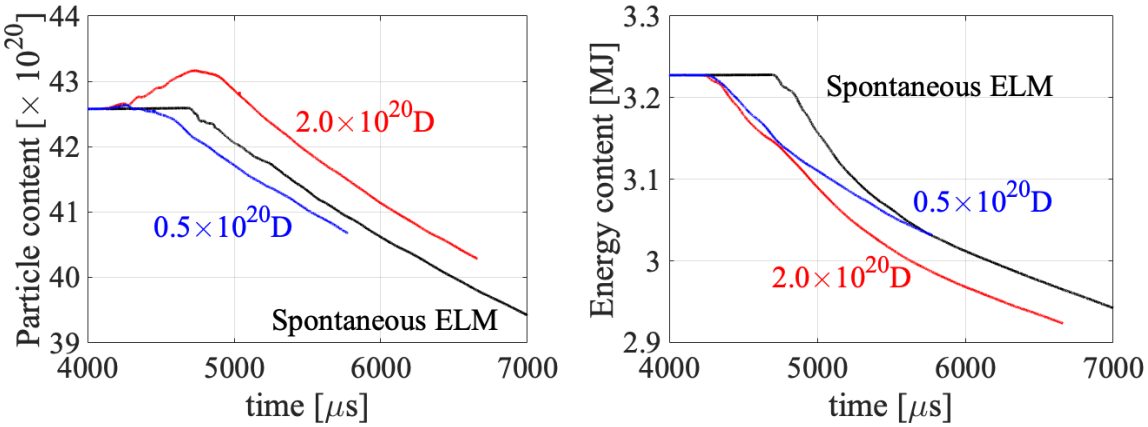

Figure 17a. The particle content of the inside of the separatrix versus time.
Figure 17b. The energy content of the inside of the separatrix versus time.

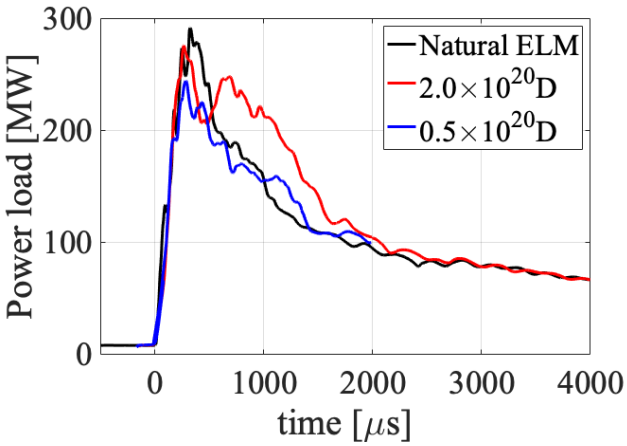

Figure 18. The total power load onto the divertor and the wall versus time. The time is justified with the time of the ELM onset for all cases.

Figure 19 shows the radial profile of the heat flux on the inner and the outer divertor target versus time for two pellet sizes, $0.5\text{x}10^{20}$D and $2.0\text{x}10^{20}$D. The both sizes of pellet injection shows the multiple peaks of the radial profile of the heat flux during the pellet triggered ELM. During the ELM event, the heat flux also appears in the inner divertor target. This is due to the plasma rotation induced by the pellet triggered ELM in poloidal direction, i.e. the finger-like ballooning mode structures appearing in LFS are transported to the HFS due to the plasma rotation of the counter-clock direction. The particle and the heat transport along the magnetic field lines also contributes the observation. The stochastic layer of the edge region is connected with both outer and inner divertors through the magnetic field lines therefore the ELM filament structures which appeared in the region of outer divertor target can reach to the inner divertor target.

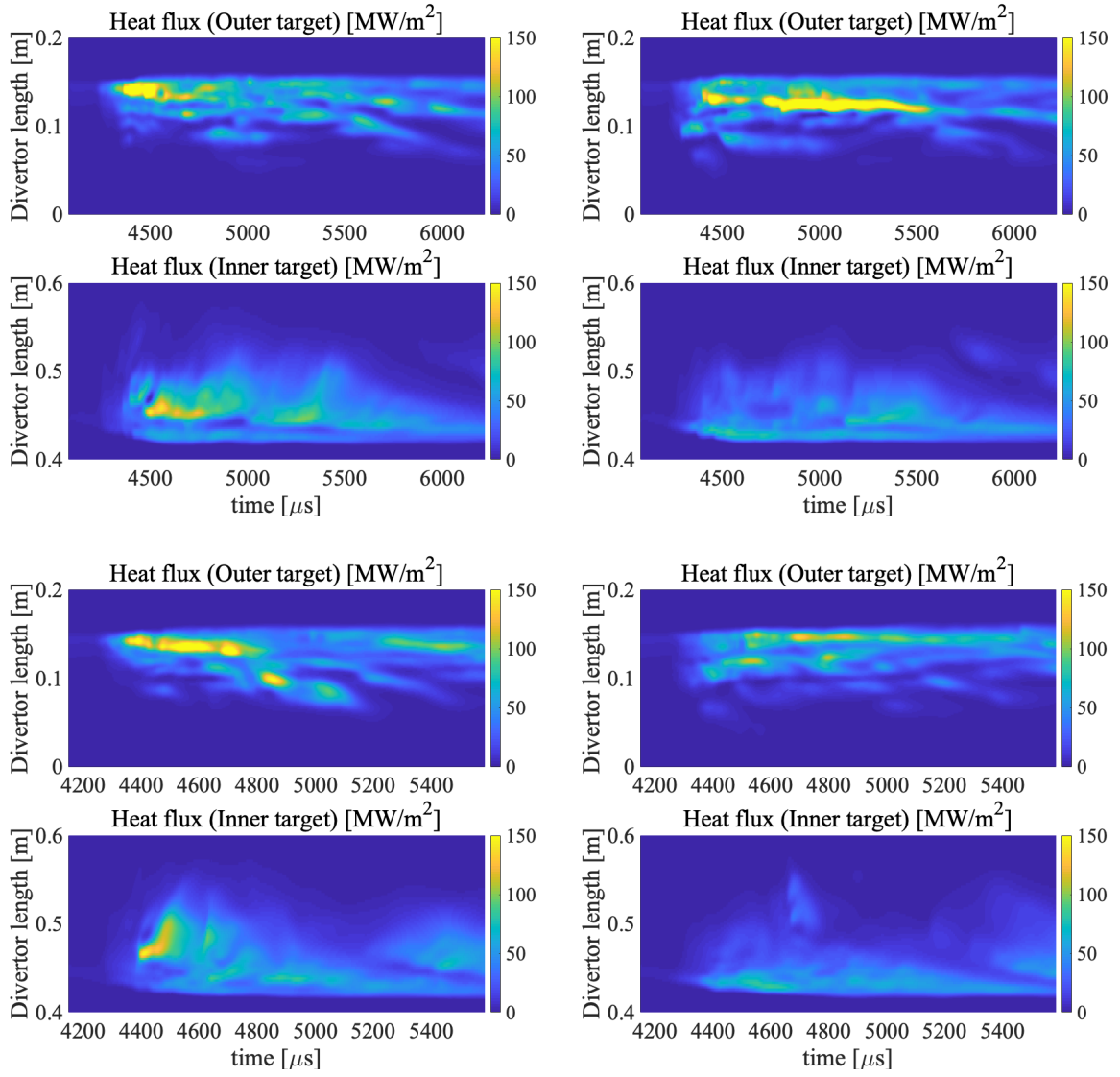

Figure 19. The time evolution of the radial profile of the heat flux on the inner and the outer divertor target. The 2.0x10^{20}D pellet is shown in the top panels and the 0.5x10^{20}D pellet is shown in the bottom panels, for (left) toroidal angle = 180^o and (right) toroidal angle = 0^o which is the pellet injection location.

Figure 20 shows the radial profile of the heat flux on the outer divertor target during the spontaneous ELM and the pellet triggered ELMs, at the toroidally opposite locations, toroidal angle = 180^o and toroidal angle=0^o where the toroidal location of pellet injection. The radial profile of the heat flux on the divertor target is toroidally asymmetric in the pellet triggered ELMs as shown in Fig. 20. This is due to that the pellet injection as the pellet injection breaks the toroidal axisymmetry of the tokamak plasma. The observation of the toroidal asymmetry of the power flux to the divertor during the pellet triggered ELM is consistent with the observation in experiments at JET [Wenninger 2011].

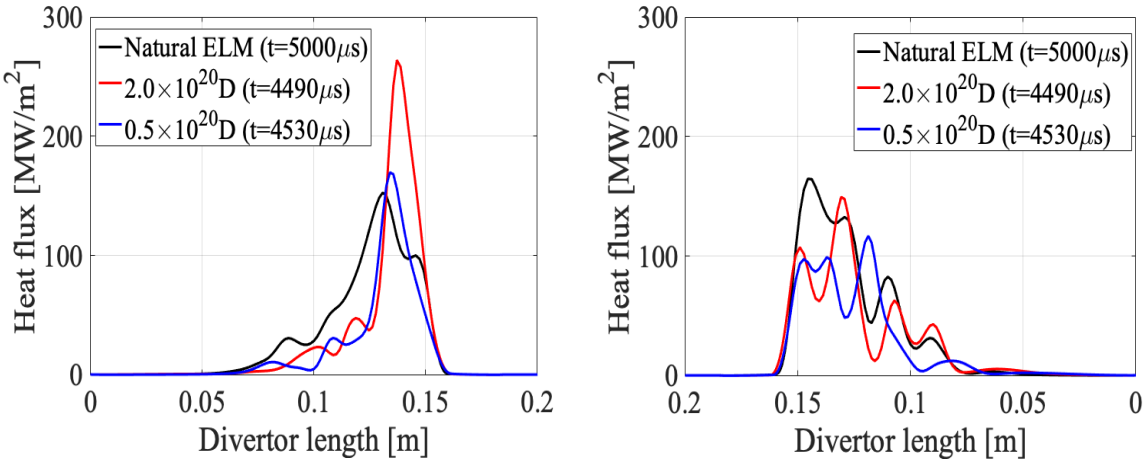

Figure 20. Profiles of the maximum divertor heat flux on the outer target at the toroidally opposite locations, (left panel) toroidal angle = 180º and (right panel) toroidal angle=0º where the toroidal location of pellet injection.

4.3. Comparison with the experiment

The analysis of divertor power load footprint of pellet-triggered and spontaneous ELMs on the outer divertor target plate for the JET shot 84690 is reported in [Frigione 2015]. This analysis was performed with the aid of a fast resolution infra-red (IR) camera. The time resolution of this instrument was 100-300 μs, depending on the view area, while the spatial resolution on the region of interest was 1.6mm [Eich 2011, Balboa 2012]. The IR camera is located at a toroidal angle of 90º from the pellet injection system (the angle coordination is defined as the clockwise direction from the top view of the tokamak) as shown in Fig. 21. There are two infrared diagnostics (KL9B, KL3B) available in JET [Balboa 2012] but for this particular experiment only one of them provided good quality data for the analysis, and additional comparison using the two cameras can be put as part of the future work. In the experiment analysis, the power flux is plotted as a function of major radius and time-averaged heat flux during the ELM event as shown in Fig. 5 of [Frigione 2015].

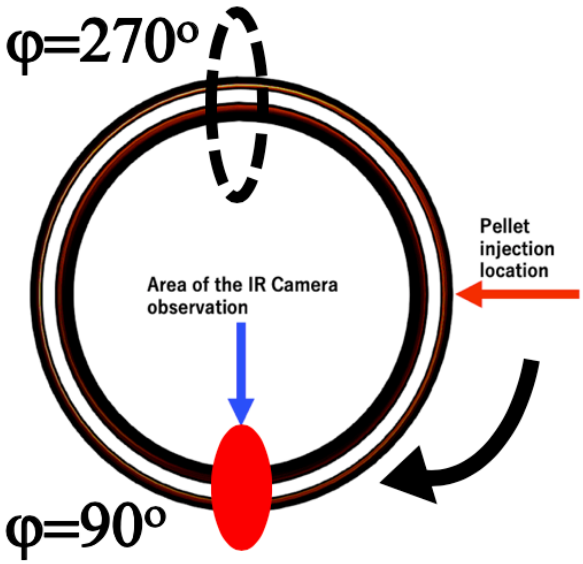

Figure 21. The schematic picture of the divertor target from the top view of JET tokamak. The locations of the pellet injection and the area of the IR camera observation are indicated.

Validation of the JOREK simulations is obtained by comparing the results against the divertor heat flux profile obtained from IR camera data. The JOREK simulations show the radial position of the strike point of the outer target is R=2.70 [m]. The time-averaged heat flux over the ELM events of the pellet triggered ELM ($0.5x10^{20}$D pellet) and the spontaneous ELM is shown in Fig. 22 at the same toroidal location as the experiment IR camera. The time window of averaging process is performed over the ELM event, for the spontaneous ELM (4680-5150μs) and the pellet triggered ELMs (4280-4550μs). Both of the ELMs show the similar heat flux onto the PFC, ~60 MW/m^2 which is similar value with the experiment observation [Frigione 2015]. The wetted area (the width of the heat flux profile which is defined at over than 10 MW/m^2) of JOREK simulation is 5.0 cm for the pellet triggered ELM and 6.5 cm for the spontaneous ELM. The wetted area of the JOREK simulation shows narrower than the experiment result.

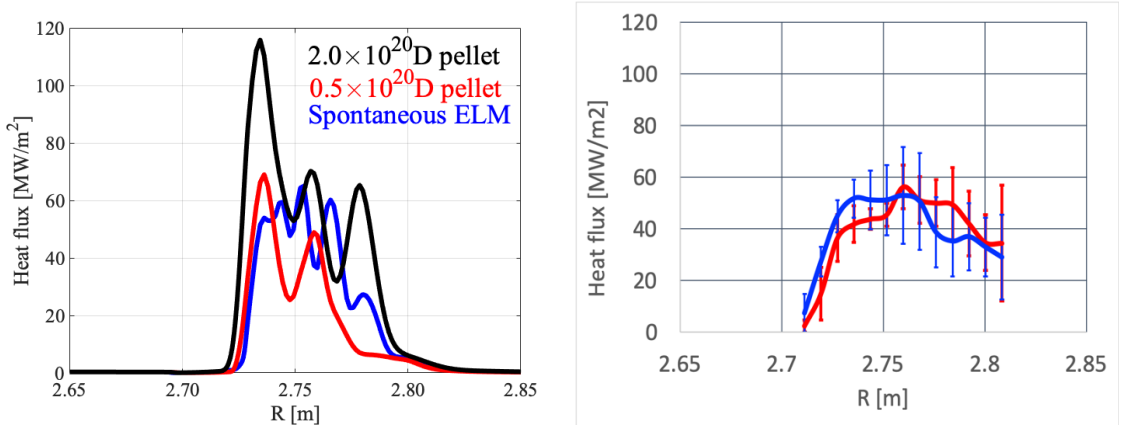

Figure 22. The heat flux onto the outer divertor target of the (Left panel) JOREK simulation and (Right panel) the experimental data [Frigione 2015]. The heat flux profile is averaged over the ELM event. The time window of averaging process is performed over the ELM event, for the spontaneous ELM (4680-5150μs) and the pellet triggered ELMs (4280-4550μs). Blue lines show the spontaneous ELM, the red lines show the triggered ELM by $0.5x10^{20}$D pellet and the black line shows the triggered ELM by $2.0x10^{20}$D pellet which is nominal value for experiment.

The location of the JET IR camera is at the toroidal angle of 90° as shown in Fig. 21. This is the only location which we can observe the experiment data of the heat flux. The JOREK simulations can also estimate the heat flux at the opposite side of the camera location. Figure 23 shows the time-averaged heat flux at the toroidal angle of 90° where the location of the IR camera and the angle of 270° which is the toroidally opposite side of the camera location. The spontaneous ELM shows the similar value of the time-averaged heat flux, ~60 MW/m^2 for any toroidal angles as the spontaneous ELM is toroidally symmetric behaviour. However, the pellet triggered ELMs show a toroidally asymmetric behaviour, the pellet of $0.5x10^{20}$D shows that the heat flux of ~60 MW/m^2 at the IR camera location is similar to the spontaneous ELM. On the other hand, the toroidally opposite side shows up to ~120 MW/m^2 which is factor 2 larger than the observation of IR camera on the other side of the tokamak. Figure 24 shows the 3D contour plot of the heat flux profile onto the outer divertor target versus the major radius R and the whole toroidal angle from 0°to 360° in the case of $0.5x10^{20}$D pellet. At the location of the IR camera which is the toroidal angle of 90° shows the heat flux of ~60 MW/m^2 at close to the strike point R=2.70 m. The toroidal location of the angle of 270° shows the factor 2 larger heat flux and the peak point of the heat flux profile is R=2.80 m which is shifted to the outer direction about 10 cm from the strike point. The agreement between JOREK simulations and JET experiments can be found different

condition, with the pellet 2.0x10^{20}D triggered ELM. The most part of the heat flux in the order of 60MW/m^2 as similar with the pellet size of 0.5x10^{20}D and the spontaneous ELM. In this work, the plasma is unstable, therefore any size of the pellet can trigger an ELM. The pellet triggered ELM occurs when the pressure perturbation by pellet injection reaches a critical perturbation level. The ELM size will not be very different in this condition. This work highlights the benefit of having a larger number of IR cameras to analyse the heat flux for the experiments which are assumed to be toroidally asymmetric, such as the pellet and/or gas injection experiments.

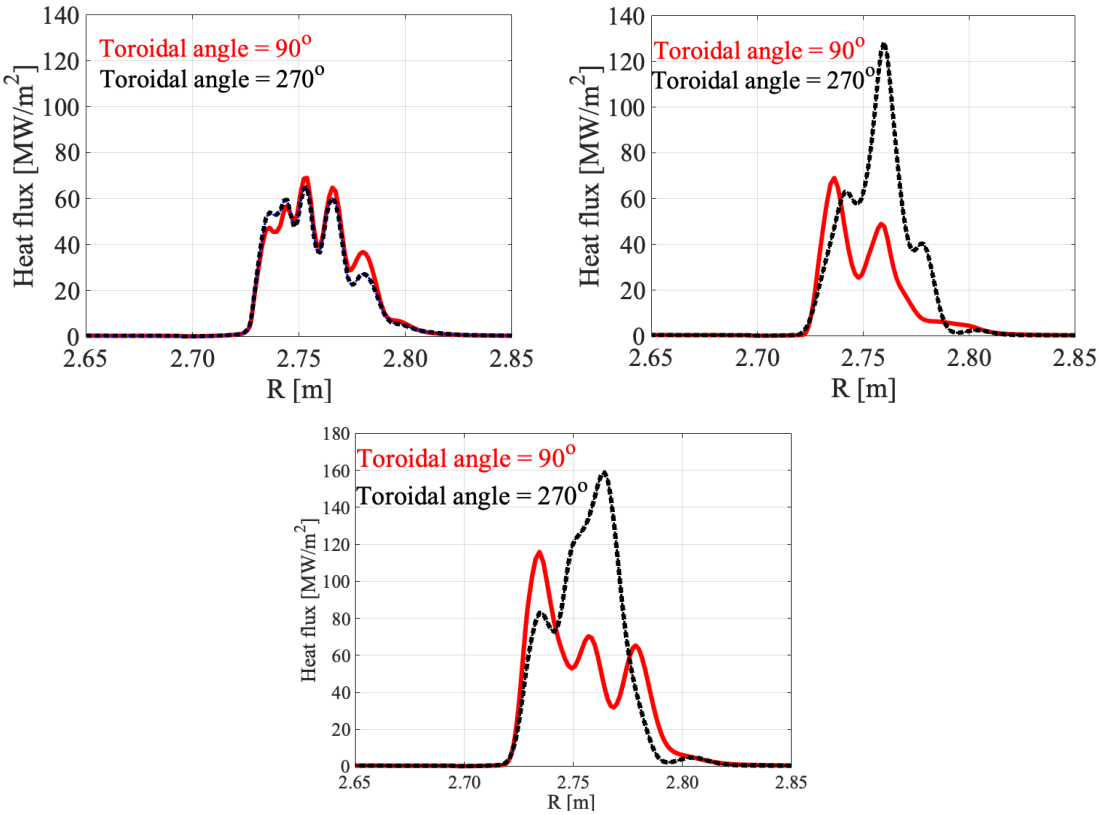

Figure 23. The time-averaged heat flux over the ELM event onto the outer divertor target of the JOREK simulation. Top-left panel shows the spontaneous ELM, the top-right panel is 0.5x10^{20}D pellet triggered ELM and bottom panel is 2.0x10^{20}D pellet triggered ELM. The red lines show the toroidal angle of 90° where the IR camera detects the power load. The dashed-black lines show the angle of 270° which is the toroidally opposite side of the camera location which cannot be observed via experiment and can be much higher.

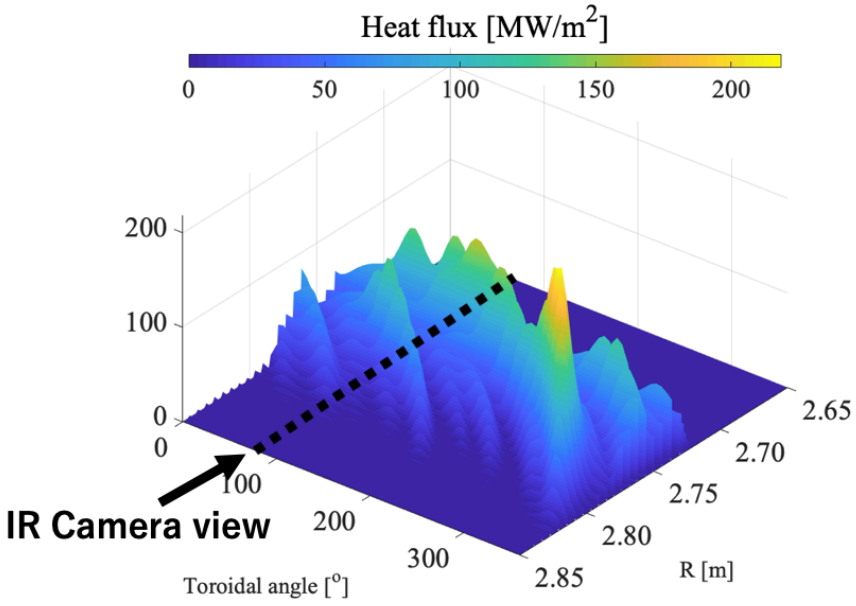

Figure 24. The 3D contour plot of the heat flux profile onto the outer divertor target versus the major radius R and the whole toroidal angle from 0^{o}to 360^o in the case of 0.5x10^{20}D pellet.

5. Summary and Conclusions.

Modelling of the ELM triggering by pellet injection with JOREK for JET has been carried out. In consistent with the observation in JOREK simulation of DIII-D plasma, the 3D pressure perturbation due to the pellet ablation excites medium/high-n ballooning modes. The simulation analysis shows that both of the pellets (0.5x10^{20} D and 2.0x10^{20} D) act as an ELM pacing pellet when the plasma is very unstable. The understanding of the ELM mitigation is more important in the "local" power load onto the divertor target. The JOREK simulations show the good agreement with the experiment observation [Frigione 2015] in terms of the similar heat flux onto the PFC, ~60 MW/m^2. The order of the peak of the heat flux are similar in between the spontaneous ELM and the pellet triggered ELM. In this work, the toroidal angle of 90^o where the location of the IR camera and the angle of 270^o which is the toroidally opposite side of the camera location are estimated. The spontaneous ELM shows similar values of the time-averaged heat flux, ~60 MW/m^2 for any toroidal angles as the spontaneous ELM has a toroidally symmetric behaviour. However, the pellet triggered ELMs show a toroidally asymmetric behaviour, the pellet of 0.5x10^{20}D shows that the heat flux of ~60 MW/m^2 at the IR camera location. On the other hand, the toroidally opposite side shows up to ~120 MW/m^2, a factor 2 larger than the observation of IR camera which cannot see this toroidal location. This work highlights the benefit of having a larger number of IR cameras to analyse the heat flux for the experiments which are assumed to be toroidally asymmetric, such as the pellet and/or gas injection experiments. This study shows that more work needs to be done to certify the efficiency of pellet pacing in terms of divertor heat flux mitigation. The toroidally asymmetric profile of heat flux onto the divertor target due to the pellet injection has been observed in the previous work of DIII-D [Futatani 2014] in agreement with the present JET simulation results. The toroidal angle position of the peak heat flux depends on the q-profile, i.e. configuration of the magnetic fields as the pressure perturbation propagates along the magnetic field lines. Therefore, control of q_{95} may be a potential application for ELM control as the toroidal location of divertor erosion depends on q_{95}. This will be a subject of further studies. The next important step is to investigate the

pellet triggered ELM in the presence of realistic plasma flows including diamagnetic drift, neoclassical effects, and toroidal rotation which has been neglected in this paper. In the proceedings of IAEA-FEC 2016 [Futatani 2016], the work assumes to inject the pellets after the ELM event, i.e. in a very stable plasma, to study the dependence of the pellet sizes on the probability of ELM triggering, including the smaller and the larger pellets than the capacity of the JET pellet injector. In the work presented here, the aim is to study the difference in divertor heat-fluxes between pellet-triggered ELMs and spontaneous ELMs, for similar MHD stability. In order to combine both these works, the inclusion of the realistic flow and the plasma parameters of higher Lundquist number would be required to perform more advanced simulations which would be more capable to carry out quantitative comparison, by modelling both the pellet triggering of stable plasmas, as well as heat-flux comparisons.

Acknowledgement
The work of S.F. is supported by a Ramón y Cajal grant from the Spanish Ministry of Economy and Competitiveness (RYC-2014-15206). This work has been carried out within the framework of the EUROfusion Consortium and has received funding from the Euratom research and training programme 2014-2018 and 2019-2020 under grant agreement No 633053. The views and opinions expressed herein do not necessarily reflect either those of the European Commission. The author thankfully acknowledges the computer resources of PRACE (Partnership for Advanced Computing in Europe) and RES (Spanish Supercomputing Network) at MareNostrum and the technical support provided by Barcelona Supercomputing Center, and the support from Marconi-Fusion, the High Performance Computer at the CINECA headquarters in Bologna (Italy) for its provision of supercomputer resources.

References

[Aiba 2017] N. Aiba et al., Plasma Phys. Control. Fusion 60, 014032 (2018)

[Balboa 2012] I. Balboa et al., Rev. Sci. Instrum. 83 (2012) 10D530.

[Baylor 2013] L. Baylor et al., Physics of Plasmas 20, 082513 (2013).

[Eich 2007] T. Eich et al., Plasma Phys. Control. Fusion 49, (2007) 573-604.
[Eich 2011] T. Eich et al., J. Nucl. Mater. 415 (2011) S856–S859.

[Eich 2017] T. Eich et al., Nuclear Materials and Energy 12 (2017) 84-90.

[Frassinetti 2017] L. Frassinetti *et al* 2017 *Nucl. Fusion* **57** 016012.
[Frigione 2015] D. Frigione et al., Journal of Nuclear Materials 463, 714 (2015).

[Futatani 2014] Futatani S., et al., Nucl. Fusion **54** 073008 (2014)

[Futatani 2016] S. Futatani, et al., "Non-linear MHD Simulations of Pellet Triggered ELMs" Preprint: 2016 26th IAEA Fusion Energy Conference, Kyoto, TH/P1-25. (https://nucleus.iaea.org/sites/fusionportal/Shared%20Documents/FEC%202016/fec2016-preprints/preprint0186.pdf)

[Gal2008] Gal, K., et al., Nucl. Fusion **48** (2008) 085005.

[Garzotti 1997] L. Garzotti et al., Nucl. Fusion **37**, 1167 (1997).

[Houlberg1988] Houlberg, W., et al., Nucl. Fusion **28** (1998) 595.

[Huysmans2009] Huysmans, G.T.A., et al., Plasma Phys. Control. Fusion **51** (2009) 124012.

[Lang2003] Lang, P.T., et al. Nucl. Fusion **43** (2003) 1110.

[Lang2013] P.T. Lang et al., Nucl. Fusion **53** (2013) 073010.

[Loarte 2014] Loarte, A., et al., Nuclear Fusion, 54, 033007 (2014).

[Mink 2018] A. F. Mink et al., Nuclear Fusion 58, 026011 (2018).

[Pamela 2017] Pamela S.J.P., et al., Nucl. Fusion 57 076006 (2017).

[Parks1978] Parks, P.B., et al., Phys. Fluids **21** (1978) 1735.

[Perez von Thun 2019] C. Perez von Thun et al., Nuclear Fusion 59, 056004 (2019)

[Orain 2015] F. Orain, et al., Phys. Rev. Lett. 114, 035001 (2015).

[Orain 2016] Orain F., et al., Nuclear Fusion 57, 022013 (2016)

[Wenninger2011] Wenninger, R.P, et al., Plasma Phys. Control. Fusion **53** (2011) 105002.